



**E-Infrastructures
H2020-EINFRA-2015-1**

**EINFRA-5-2015: Centres of Excellence
for computing applications**

EoCoE

**Energy oriented Center of Excellence
for computing applications**

Grant Agreement Number: EINFRA-676629

D4.2 - M22

**Analysis of temperature ranges and fluid flow rates
in a 3D subsurface model.**

Project and Deliverable Information Sheet

EoCoE	Project Ref:	EINFRA-676629
	Project Title:	Energy oriented Centre of Excellence
	Project Web Site:	http://www.eocoe.eu
	Deliverable ID:	D4.2 - M22
	Lead Beneficiary:	Juelich
	Contact:	Jan Niederau
	Contact's e-mail:	jniederau@eonerc.rwth-aachen.de
	Deliverable Nature:	Report
	Dissemination Level:	PU*
	Contractual Date of Delivery:	M22 31/07/2017
	Actual Date of Delivery:	M24 04/09/2017
	EC Project Officer:	Carlos Morais-Pires

* - The dissemination level are indicated as follows: PU – Public, CO – Confidential, only for members of the consortium (including the Commission Services) CL – Classified, as referred to in Commission Decision 2991/844/EC.

Document Control Sheet

Document	Title :	Analysis of temperature ranges and fluid flow rates in a 3D subsurface model.
	ID :	D4.2 - M22
	Available at:	http://www.eocoe.eu
	Software tool:	SHEMAT-Suite
Authorship	Written by:	Jan Niederau
	Contributors:	Johanna Bruckmann, Henrik Büesing
	Reviewed by:	Nathalie Girard, Edouard Audit

Contents

1	Introduction - Motivation	5
2	Database	5
2.1	Geological data	6
2.2	Groundwater data	6
2.3	Temperature data	6
3	Petrophysical data	7
4	Geological Background	9
4.1	Geological model	9
5	Numerical Model	10
6	Results	12
6.1	Calibration and influence of paleoclimate	12
6.2	Temperature ranges	14
6.3	Variations in groundwater flow	16
7	Conclusion	17

List of Figures

1	Conceptual workflow of Task 4.1 and Task 4.2. Deliverable 4.2 comprises the first three steps, yielding parameters for the BHE Model, which is the focus of Task 4.2.	5
2	Map of the study area showing available well data. The three polygons represent different model boundaries. The geometry of the numerical flow model (orange square) are extracted from the regional geological model (red square).	6
3	Map with groundwater table contour lines. The groundwater tables for both, shallow and deeper aquifer suggest a regional flow from south to north.	7
4	Plot of temperature vs depth for available temperature data sources. All temperature profiles show significant changes in gradient at certain depths, suggesting the occurrence of lignite seams with a low thermal conductivity.	7
5	Permeability distributions for the three major aquifers and one major aquitard in the flow model.	8

6	Experimental semivariogram of the Liegendsande Aquifer. The sill is reached at around 1100 m lag distance, which is used as the correlation length for this aquifer.	9
7	Geological model of the tertiary sediments in the study area. Paleozoic sediments are depicted in gray. The model covers an area of 16 km ² (the flow model box in Fig. 2).	10
8	Comparison of parsing duration for different SHEMAT-Suite input file sizes. Left: Input file size of 2.1 MB, parsing with different number of cores. Right: Input file size of 229 MB, serial parsing.	12
9	Comparison of simulated temperatures at different boreholes with observation data.	13
10	(left) comparison of simulated temperatures with measurements in the borehole Teveren.(right) slice through the calibration model, showing position of the borehole and the simulated temperature field.	13
11	a) correction of discrepancy in temperature response by considering paleoclimatic changes. b) assigned temperature - trend for the transient simulation (modified from Clauser & Mareschal (1995)).	14
12	xy presentation of observation points in the model. Variances in groundwater level are derived from seasonal time-series of measurements. Black numbers are IDs of monitoring points.	15
13	Mean and standard deviation of a priori and a posteriori distributions in simulated temperatures at three selected monitoring points (see Fig. 12 for location).	16
14	Mean and standard deviation of a posteriori y-direction velocity field in about 30 m depth below surface.	17
15	Mean and standard deviation at monitoring points	17

List of Tables

1	Geological units and ascribed petrophysical properties which were used in the hydrothermal flow model.	8
2	Boundary conditions of the initial flow model. Top temperature is calculated as a function of altitude (z), lapse rate ($t = -0.0065$), and average surface temperature ($t_{surface} = 11$ °C). Surface temperatures change in time according to Fig. 11 b). Initial specific heat flow of 0.045 [W m ⁻¹ K ⁻¹] changed to 0.014 [W m ⁻¹ K ⁻¹] based on inversion results.	11

1. Introduction - Motivation

Deliverable 4.2 covers the progress of work done in Task 4.1 of workpackage 4. This task aims at generating a detailed 3D geological model of the subsurface of the city of Geilenkirchen. Geologically speaking, this area belongs to the lower Rhine Embayment and comprises tertiary sediments unconformably overlying carboniferous sediments. Neu-Teveren, a settlement adjacent to the NATO-Airbase of Teveren, is planned to be fully restructured within the next years. In the course of reconstruction, space heating and cooling by geothermal direct heat supply is one option, which will be presented to potential stakeholders.

In order to provide estimates of expected temperature at depth, and groundwater flow velocity, we discretize the detailed 3D geological model for simulating temperature and groundwater flow, while considering a heterogeneous underground. The heterogeneity within the underground is studied by stochastic simulations, where we vary the petrophysical parameter of the main aquifer units in the study area. By this, we can provide an uncertainty connected to average temperatures and groundwater flow rates simulated by our model.

As the model needs to resolve even thin geological units, it consists of more than 8 million grid nodes, covering an area of about 13.3 km². We run this model on JURECA (Juelich Research on Exascale Cluster Architectures) using the code SHEMAT-Suite.

The following sections describe the work done in Task 4.1, according to the workflow visualized in Fig. 1.

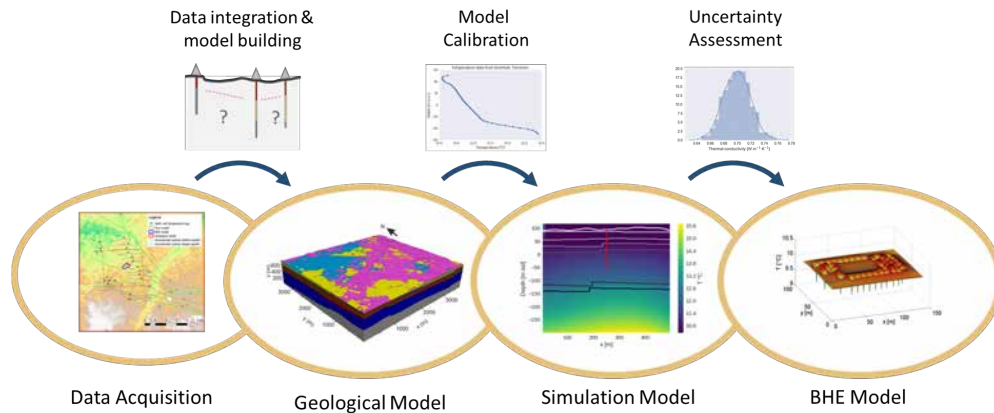


Figure 1: Conceptual workflow of Task 4.1 and Task 4.2. Deliverable 4.2 comprises the first three steps, yielding parameters for the BHE Model, which is the focus of Task 4.2.

2. Database

In preparation for creating a geological and a numerical model of the subsurface of Geilenkirchen, we built an extensive database, comprising all accessible temperature, geological, hydrogeological, and petrophysical data. Temperature and hydrogeological data are used for calibrating the numerical model. Geological data is used for creating the geological model. Petrophysical data is used for populating the numerical model and setting up an ensemble for monte carlo simulations. Fig. 2 shows the locations of measurement points for the different data types (triangles = data on groundwater level; circles = data on stratigraphy; stars = temperature measurements) in the study area.

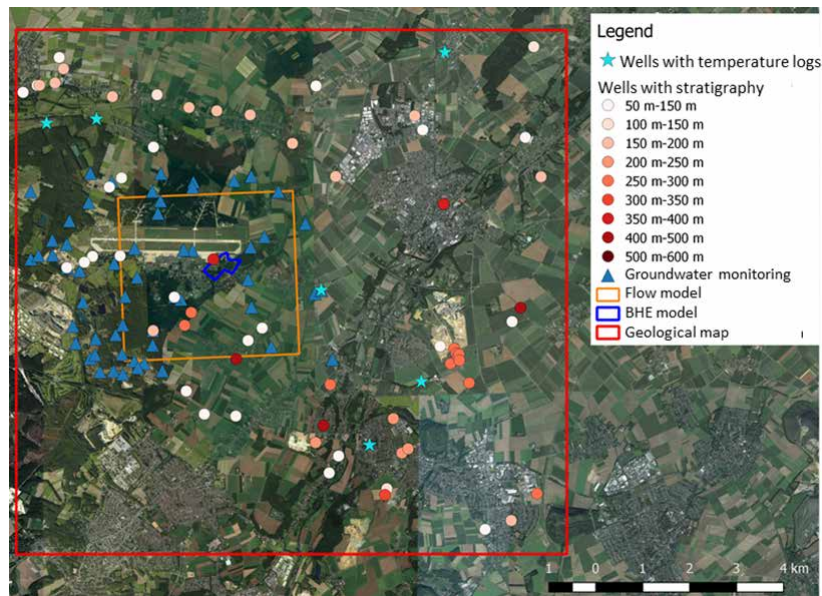


Figure 2: Map of the study area showing available well data. The three polygons represent different model boundaries. The geometry of the numerical flow model (orange square) are extracted from the regional geological model (red square).

2.1 Geological data

Geological data was provided by the geological survey of North Rhine-Westphalia, and mainly comprises stratigraphy from boreholes (see Fig. 2), geological cross-sections and maps, as well as structural maps. A digital elevation model (DEM) was obtained from the ASTER Global Digital Elevation Model V002 (ASTER GDEM is a product of METI and NASA). Geological data was georeferenced in one coordinate system as preparation for loading the data in the geological modeling software.

2.2 Groundwater data

Groundwater data was provided by the Erftverband. It comprises isohypses of the groundwater table (Fig. 3), hydrograph curves, data on groundwater table from various monitoring wells, and hydraulic conductivities of the main aquifers and aquitards. The groundwater isohypses were interpolated and then used as a top boundary condition for the numerical flow model. Hydrographs show a continuous decline in groundwater table, presumably due to mining activities in open lignite pits in the SE of the study area. Hydraulic conductivities were converted to permeabilities, and their specified ranges were used as a proxy to create permeability distributions of the major aquifer units.

2.3 Temperature data

Temperature data in form of temperature logs of multiple boreholes is available in the study area (stars in Fig 2). The temperatures are used to calibrate the specific heat flow of a regional scale model, which is then applied as basal boundary condition to the flow model (orange square in Fig. 2). The temperature logs (Fig. 4) show significant deviations from a linear geothermal gradient.

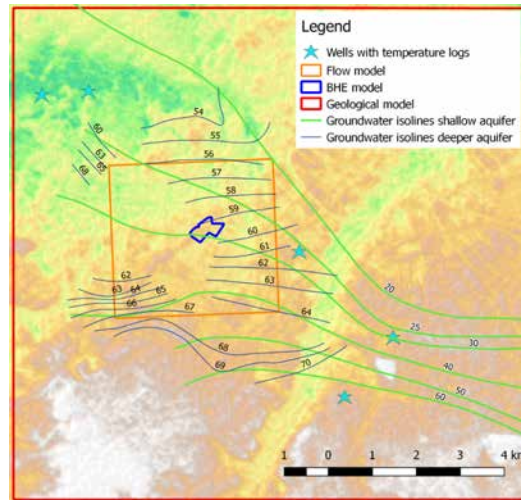


Figure 3: Map with groundwater table contour lines. The groundwater tables for both, shallow and deeper aquifer suggest a regional flow from south to north.

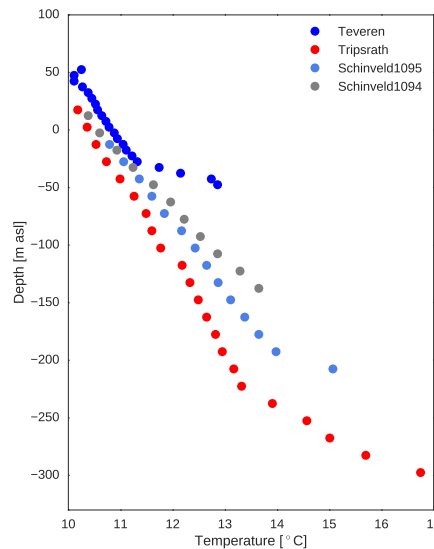


Figure 4: Plot of temperature vs depth for available temperature data sources. All temperature profiles show significant changes in gradient at certain depths, suggesting the occurrence of lignite seams with a low thermal conductivity.

Multiple reasons may cause such variations, among others: different thermal conductivities of the subsurface, significant (vertical) advective heat transport, or the influence of a paleo-climate signal. The strong changes, e.g. at around 140 m depth in the boreholes Teveren suggest the occurrence of lignite seams. Lignite has a very low thermal conductivity, thus acts as a thermal insulator in the subsurface.

3. Petrophysical data

Data on petrophysical parameters of the main lithological were collected from different sources. Some Porosity and permeability data for the main aquifer units were taken

from a mining region model by RWE Power AG. Jorand et al. (2015) provide an extensive statistical database for rock thermal conductivity (λ), specific heat capacity (c_p), porosity (ϕ), and density (ρ) for lithologies encountered in lower rhine embayment. They measured many of those properties along a borehole close to the study area. We used mixture laws for estimating average petrophysical parameters for the aquifer and aquitard units in our model. Table 1 summarizes the mean parameters for each model unit.

Table 1: Geological units and ascribed petrophysical properties which were used in the hydrothermal flow model.

Model Unit	Porosity (<i>apriori</i> <i>aposteriori</i>)		vertical Permeability (m ²)	Thermal Conductivity (<i>apriori</i> <i>aposteriori</i>) (matrix; W m ⁻¹ K ⁻¹)	
Quaternary Aquifer	0.22	<i>0.203</i>	$1.01 \cdot 10^{-10}$	2.0	<i>2.34</i>
Upper Rotton	0.33	-	$3.7 \cdot 10^{-16}$	1.88	<i>1.88</i>
Hauptkies Aquifer	0.28	<i>0.239</i>	$1.19 \cdot 10^{-10}$	2.0	<i>2.63</i>
Seam Schophoven	0.33	<i>0.303</i>	$2.5 \cdot 10^{-16}$	0.7	<i>0.95</i>
Inden Layers & Ville Layers	0.2	<i>0.193 & 0.205</i>	$1 \cdot 10^{-13}$	2.5	<i>2.78 & 2.3</i>
Seam Morken	0.13	0.115	$1.32 \cdot 10^{-16}$	0.7	<i>0.15</i>
Koeln Layers & Grafenberg Layers	0.11	<i>0.109</i>	$3.41 \cdot 10^{-13}$	2.5	<i>2.51</i>
Liegendsande Aquifer	0.11	<i>0.11</i>	$2.18 \cdot 10^{-13}$	2.5	<i>2.5</i>
Paleozoic Basement	0.1		$1.18 \cdot 10^{-16}$	3.78	

Apriori values for thermal conductivity were assessed by performing a gradient based inversion using temperature data from the Teveren borehole (blue in Fig. 4). Thermal conductivity of Seam Morken has the highest sensibility on the simulation results, as it causes the steep temperature gradient visible in the Teveren borehole. Its aposterior thermal conductivity of $0.15 \text{ W m}^{-1} \text{ K}^{-1}$ is likely too low, although it fits the data best. A more detailed description can be found in subsection 5-code. We assessed means and

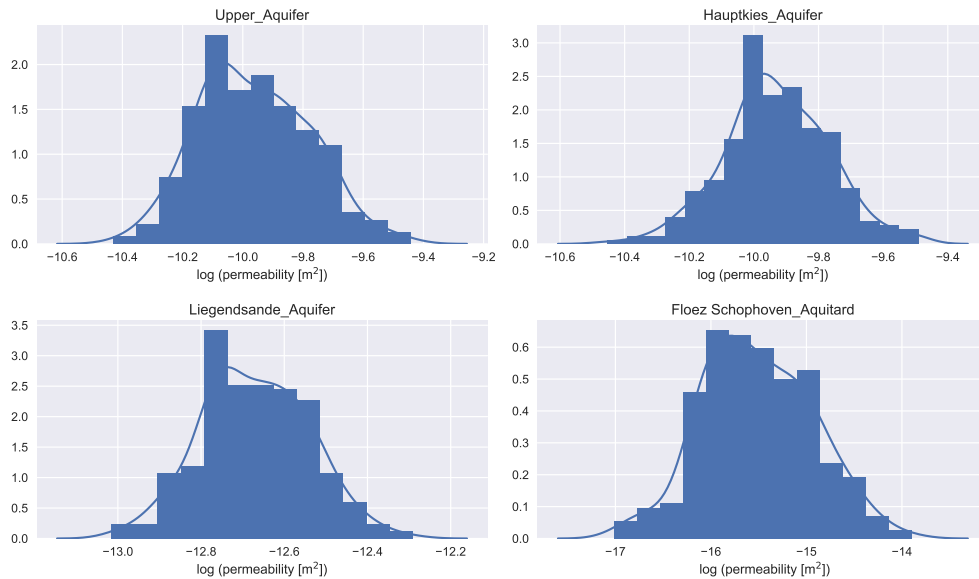


Figure 5: Permeability distributions for the three major aquifers and one major aquitard in the flow model.

standard deviations for porosity, permeability, and thermal conductivity data based on the provided data and information found in Jorand et al. (2015), and generated representative

distributions of these parameters for the major aquifer units (e.g. permeability Fig. 5). These distributions are later used for creating an ensemble of equally probable realizations of the subsurface in order to consider uncertainties of petrophysical parameters and their impact on temperature distributions.

However, parameter distributions alone do not suffice for populating the parameter space in a geostatistical way. That is why we assess the spatial correlation using average porosity values from different boreholes in the study area. Spatial correlation lengths are assessed for each aquifer separately, in order to consider lithological and sedimentological differences between the aquifers. Figure 6 exemplarily shows a semivariogram of porosity for the Liegensande Aquifer. Analysis of the several semivariograms yields correlation lengths of porosity for the different aquifers. Assuming porosity and permeability to be correlated in the aquifers, we use the same correlation lengths for porosity and permeability.

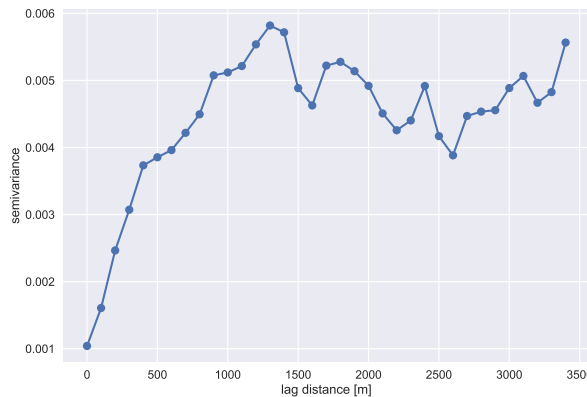


Figure 6: Experimental semivariogram of the Liegensande Aquifer. The sill is reached at around 1100 m lag distance, which is used as the correlation length for this aquifer.

4. Geological Background

The study area of the City Geilenkirchen is situated in the Lower Rhine Embayment, an active subsidence site, characterized by a NW-SE striking normal faults. This normal fault system yielded the development of a Horst-Graben-system, which created accommodation space for siliciclastic sediments from the Tertiary onwards.

The sedimentary successions consist of alternating sequences of relatively unconsolidated marine and continental deposits. The fine-grained, shale-rich marine sediments are generally less permeable than the continental deposits. In terms of the hydrogeological system, several aquifers (sandy continental deposits) are divided by less permeable lithologies (shaly marine deposits and lignite seams).

The tertiary sediments unconformably overlie consolidated Carboniferous and Devonian sediments. Those units were affected by the variscan orogeny and are significantly folded with fold axis predominantly striking NE-SW. The system of normal faults, which developed from the Tertiary onwards also dissects the palaeozoic sedimentary units.

4.1 Geological model

The geological model focuses on detailed representation of tertiary sediments in the study area. Older paleozoic units beneath the basal tertiary unconformity are grouped in

one unit in the model (grey unit in Fig. 7). Tertiary lithologies in the geological model were divided depending on their hydraulic properties, i.e. in aquifers and aquitards. Main aquifer units in the Model are the Liegendsande Aquifer, the Hauptkies Aquifer, and the quaternary sediments. Lithological units are displaced by normal faults which predominantly strike NW-SE, as mentioned before. Faults are modelled just as displacement, as there is not data on hydraulic properties of the faults.

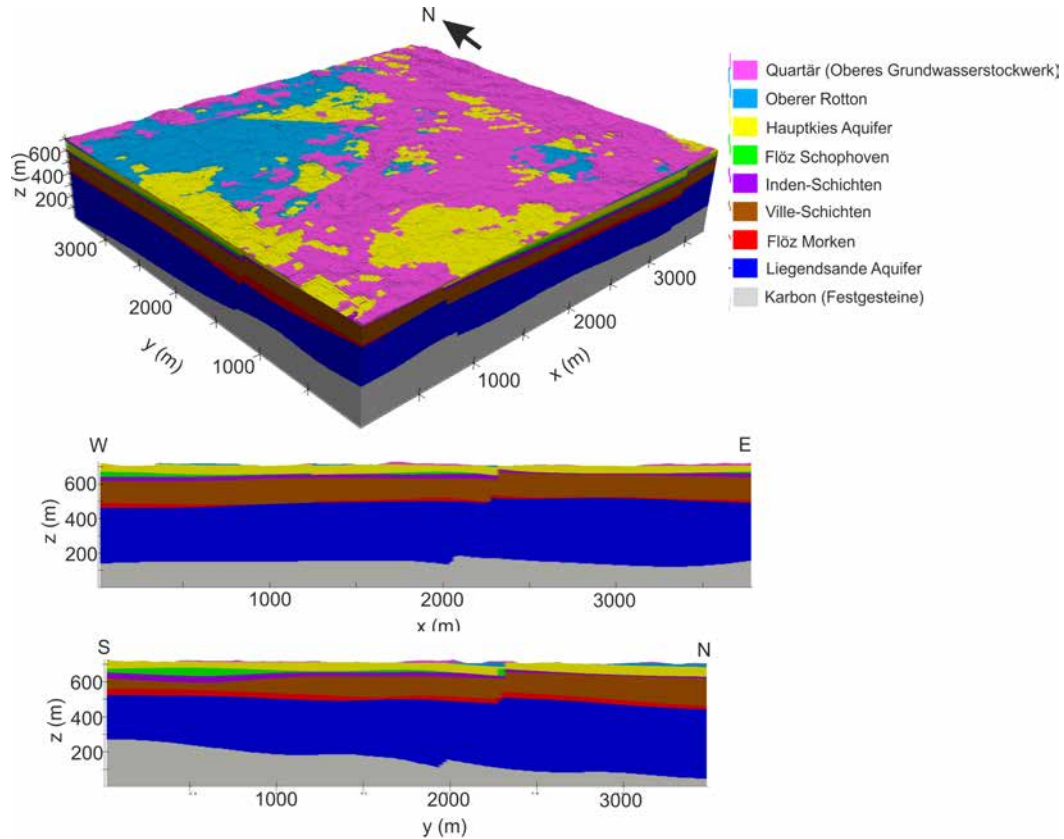


Figure 7: Geological model of the tertiary sediments in the study area. Paleozoic sediments are depicted in gray. The model covers an area of 16 km² (the flow model box in Fig. 2).

5. Numerical Model

Two numerical models were generated by discretizing the geological model in a rectangular grid. We generated one purely conductive model covering an area of 150 km² (Fig. 2 red square) for calibrating boundary conditions and petrophysical parameters (mainly thermal conductivities, see Table 1) for the model based on temperature data from the borehole Teveren. Derived parameters and boundary conditions from this model were applied to a more detailed numerical model (Fig. 2 orange square), where we solve coupled energy- and mass-balance equations, using the code SHEMAT-Suite (see section 5).

Boundary conditions

As boundary conditions have significant influence on simulation results, they should be defined as close to reality as possible. We set boundary conditions for temperature and the hydraulic potential in our flow model. Boundary conditions for the hydraulic head are set for simulating fluid flow in the model. Top and lateral boundary conditions are derived

from the water table contour lines included in our data base. For temperature boundary conditions, we chose the average surface temperature as a top boundary condition, and a reasonable specific heat flow as bottom boundary condition. Lateral boundaries for temperature are derived from conductive steady-state simulations. Table 2 summarizes the type and value of the boundary conditions applied to the model.

Table 2: Boundary conditions of the initial flow model. Top temperature is calculated as a function of altitude (z), lapse rate ($l = -0.0065$), and average surface temperature ($t_{surface} = 11$ °C). Surface temperatures change in time according to Fig. 11 b). Initial specific heat flow of 0.045 [$\text{W m}^{-1} \text{K}^{-1}$] changed to 0.014 [$\text{W m}^{-1} \text{K}^{-1}$] based on inversion results.

Parameter	Type	location	value
Temperature	Dirichlet	top	$T = z * l + t_{surface}$
Temperature	Neumann	bottom	0.045 [$\text{W m}^{-1} \text{K}^{-1}$] \rightarrow 0.014 [$\text{W m}^{-1} \text{K}^{-1}$]
Temperature	Dirichlet	lateral	result from conductive simulation
Hydraulic head	Dirichlet	top	356 m - 367 m (interpolation from isolines)
Hydraulic head	Dirichlet	lateral	356 m (north), 367 (south)

Code

As a simulation code, we use SHEMAT-Suite (Rath et al., 2006). It is derived from the SHEMAT code presented in Clauser (2003), and further developed within EoCoE. It is based on two coupled differential equations, mass- and energy-balance equation. The code can simulate heat and mass transport in hydrothermal reservoirs in steady state as well as in transient (time dependent) state. The transient flow equation used in our simulations is based on Darcy's law and the mass conservation equation:

$$S_s \frac{\partial h}{\partial t} = \nabla \left[\frac{\rho_f g \mathbf{k}}{\mu_f} (\nabla h_0 + \rho_r \nabla z) \right] + W \quad (1)$$

where ρ_f is water density [kg m^{-3}], g gravity [m s^{-2}], \mathbf{k} permeability tensor [m^2], μ_f dynamic viscosity [Pa s], h hydraulic head [m] and z the vertical coordinate in space [m]. W describes a volume source term [s^{-1}]; ρ_r is the relative density change defined by $\rho_r = \frac{\rho_f - \rho_0}{\rho_0}$, where ρ_0 is density at reference conditions (i.e. atmospheric temperature). $S_s = \rho_f g (\alpha + \phi \beta)$ [m^{-1}] is the specific storage coefficient [m^{-1}] (α and β are compressibilities [Pa^{-1}] of the rock and the fluid phase, respectively).

The heat transport equation is derived from Fourier's law $\mathbf{q} = \lambda_e \nabla T$ and the energy conservation equation:

$$(\rho c)_e \frac{\partial T}{\partial t} = \nabla [\lambda_e \nabla T] + (\rho c)_f \mathbf{v} \nabla T + H \quad (2)$$

where \mathbf{q} is specific heat flow [W m^{-2}], T is temperature [$^{\circ}\text{C}$], $(\rho c)_e$ and $(\rho c)_f$ are the effective volumetric heat capacities of the fluid-saturated porous medium and the fluid [$\text{J m}^{-3} \text{K}^{-1}$], respectively. λ_e is the tensor of effective thermal conductivity [$\text{W m}^{-1} \text{K}^{-1}$], and H is the radiogenic heat production rate [W m^{-3}]; $\mathbf{v} = \frac{\rho_f g \mathbf{k}}{\mu_f} (\nabla h_0 + \rho_r \nabla z)$ is specific discharge (or Darcy velocity) [m s^{-1}].

We used a deterministic gradient based inverse algorithm implemented in SHEMAT-Suite. The optimization problem in this algorithm is minimization of a nonlinear objective function

$$\Theta = [d - g(p)]^T C_d^{-1} [d - g(p)] + (p - p^\alpha)^T C_p^{-1} (p - p^\alpha) \quad (3)$$

p is the parameter vector, $g(p)$ is the resulting forward model, and d denotes observed data. Input values in this equation are the a priori parameters p^α , and covariance matrices of data (C_d^{-1}) and parameters (C_p^{-1}). Equation (3) is minimized iteratively using Gauss-Newton.

Cooperation with WP1

In cooperation with WP1 of EoCoE, the ASCII SHEMAT-Suite input file has been converted into a binary HDF5 format. This conversion leads to a significant performance increase in the IO phase for large input files. The needed time for input file parsing could significantly be reduced for files of usual size (1 to 3 MB, Fig. 8, left). Due to the original parsing handling of ASCII SHEMAT-Suite input files, a file had to be scanned completely for multiple times, e.g. if an optional header is not set. With the new HDF5-implementation by WP1, the input file is scanned once, avoiding this bottleneck. With really big input files, parsing time can get reduced by a factor of 100 (Fig. 8, right).

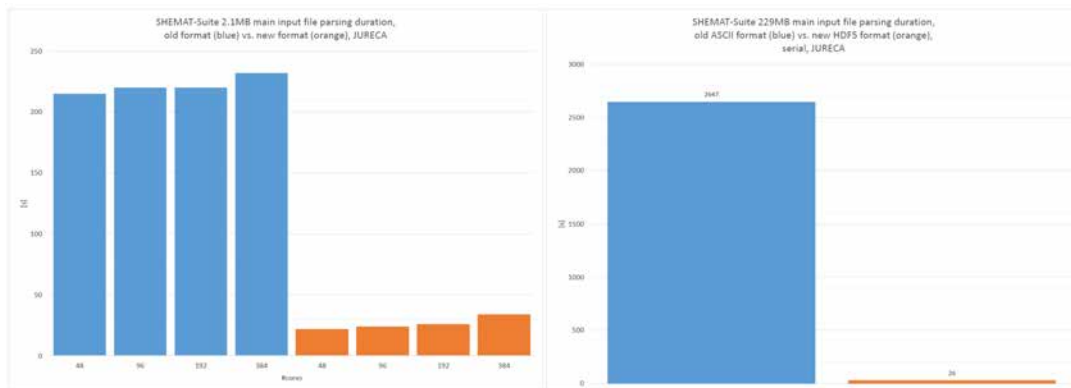


Figure 8: Comparison of parsing duration for different SHEMAT-Suite input file sizes. Left: Input file size of 2.1 MB, parsing with different number of cores. Right: Input file size of 229 MB, serial parsing.

For more information, see section 4 in EoCoE-report D1.1 *Triggered Application Support* (http://www.eocoe.eu/sites/default/files/results_files/d1.1.pdf).

6. Results

In this section, we present results from model calibration, and subsequently Monte Carlo simulations. Thermal conductivity (λ), porosity (ϕ), and boundary conditions are optimized to match observed data points from temperature logs in a calibration step. The results are then used for populating the according parameters of the flow model, and its boundary conditions.

6.1 Calibration and influence of paleoclimate

We used the previously shown temperature data as observation points for calibrating the basal specific heat flow boundary condition, as well as porosity and (matrix) thermal conductivity of the model units. For the basal boundary condition, we created a regional scale model (red square in Fig. 3). The model was calibrated using equation (3), where $g(p)$ is a steady-state, purely conductive model. Steady-state calibration of the model yielded an acceptable fit with the observed temperature data (Fig. 9). Offsets between simulated and observed temperatures, e.g. around -220 m for Tripsrath, or -46 m for Teveren are likely caused by discretization errors or changes of geological units, not sufficiently captured in

the geological model. In case of the borehole Teveren, the lignite seam with low thermal conductivity seems to be around 8 m higher in the geological model than suggested by the temperature measurements.

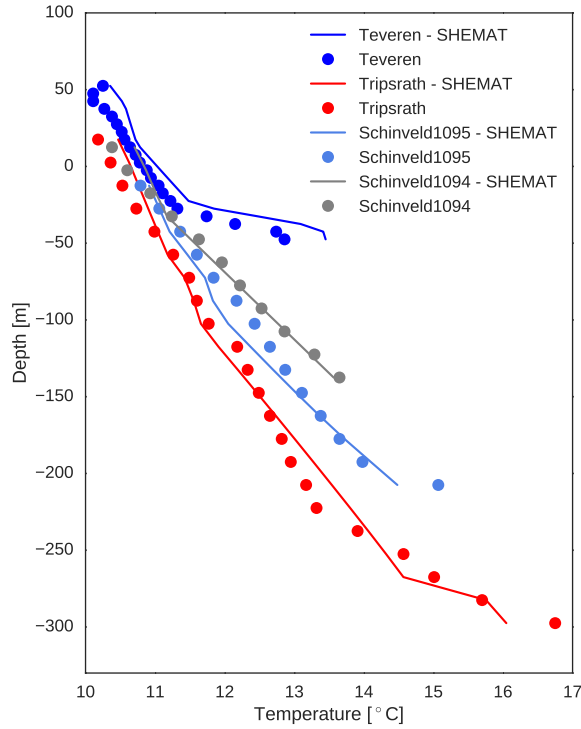


Figure 9: Comparison of simulated temperatures at different boreholes with observation data.

For assessing the impact of discretization, we built a smaller calibration model centered around the borehole Teveren. Here, simulation results show a good fit with observed temperatures (Fig. 10 left). The insulating effect of the lignite seam (Floez Morken) is presented by the temperature slice (Fig. 10 right).

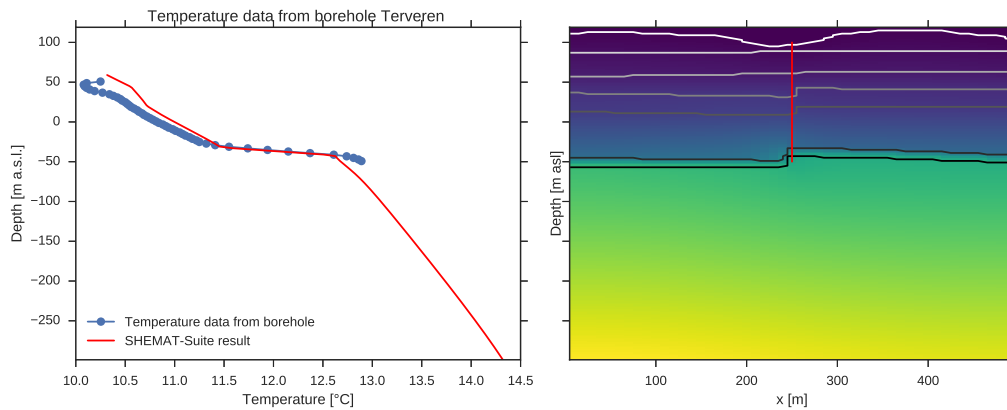


Figure 10: (left) comparison of simulated temperatures with measurements in the borehole Teveren.(right) slice through the calibration model, showing position of the borehole and the simulated temperature field.

While the influence of the lignite seam at a depth of about 50 m (below sea level), is fitted well, simulated temperatures differ above the seam. This is due the transient impact paleoclimate. Using the parameters from the steady-state calibration, we set up a transient simulation over 500 years, changing surface temperatures according to published literature data (Clauser & Mareschal, 1995). Results of the transient simulation is presented in figure 11. The assessed temperature history (Fig. 11 b) corrects the previous temperature discrepancy.

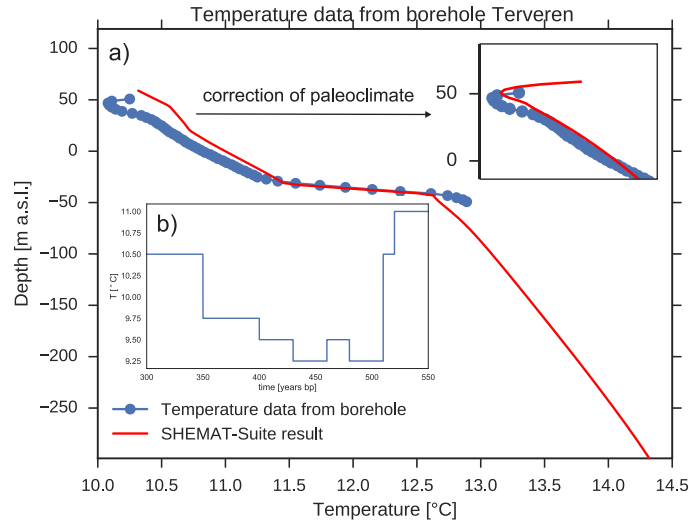


Figure 11: a) correction of discrepancy in temperature response by considering paleoclimatic changes. b) assigned temperature - trend for the transient simulation (modified from Clauser & Mareschal (1995)).

Considering transient changes in surface temperatures is important in order to assess the potential heat in place of a shallow geothermal installation, such as borehole heat exchangers (BHEs). That is why the boundary condition displayed in Fig. 11 b) has to be applied to the Monte Carlo ensemble. For the Monte Carlo simulation, we apply boundary conditions and petrophysical parameters assessed in the calibration step, i.e.:

- Porosity (ϕ), Thermal conductivity (λ)
- Specific heat flow (q) as bottom boundary condition (Neumann)
- Time dependent surface temperature (T_t) as top boundary condition (Dirichlet)

In the following, we assess temperature ranges at depths down to 300 m below sea level, as well as variance in groundwater flow. These variables are important to estimate the potential heat in place, and layout of borehole heat exchanger fields in future simulations (Deliverable D 4.3).

6.2 Temperature ranges

The Monte Carlo forward ensemble of the flow model up until now comprises multiple hundred realisations of equally likely model states after simulation time shown in Fig. 11 b. Using a rejection algorithm based on the Metropolis acceptance probability (eq. (4)),

we evaluate a posterior ensemble of realisations, based on the RMSE of each realisation ($S(z)$, $S(x_t - 1)$) normalised by the measurement error u_H .

$$\alpha(x_{t-1}, z) = \begin{cases} \exp\left(-\frac{S(z) - S(x_{t-1})}{u_H}\right), & \text{if } S(z) > S(x_{t-1}) \\ 1, & \text{otherwise} \end{cases} \quad (4)$$

That means, that the acceptance probability $\alpha(x_{t-1}, z)$ is 1 if the proposed model is better than the current model, and the proposed model gets higher acceptance. If the RMSE of the proposed model is larger than the RMSE of the current model, the proposed model is accepted with a smaller probability. u_H is assessed by error propagation of the standard deviations of the input data. We used nine boreholes with data on groundwater table as observations (Fig. 12).

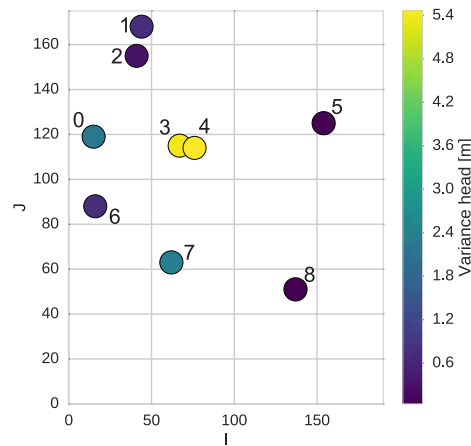


Figure 12: xy presentation of observation points in the model. Variances in groundwater level are derived from seasonal time-series of measurements. Black numbers are IDs of monitoring points.

Equation (4) yielded an acceptance probability of around 72 %. This high probability of acceptance yields an aposteriori ensemble of realizations, whose uncertainty just slightly improved compared to the apriori ensemble. Figure 13 shows temperature profiles at three exemplary monitoring boreholes (see Fig. 12 for location). Aposteriori temperature profiles have a slightly lower standard deviation than apriori profiles. Influence of the insulating lignite seam Morken is present in all realizations. Variation of temperature occurs in the upper 100 m - 150 m of the model, within two major aquifers; the Quaternary Aquifer, and the Hauptkies Aquifer.

Overall, the results suggest that the rejection algorithm was not successful in significantly increasing the certainty of the aposteriori ensemble. Multiple reasons can explain this observation. Observation points are rather close to the surface, where we applied the top boundary condition for the hydraulic head. Thus, a potential influence of the top boundary condition, which is similar for all realizations, can not be excluded. Permeability within the Hauptkies Aquifer varies between $10^{-9.4} \text{ m}^2$ and $10^{-10.4} \text{ m}^2$ (Fig. 5 top right), as deduced from available data. This narrow probability range together with a fairly big horizontal correlation length cause differences between each realization to be very small. That is, the rejection algorithm cannot be efficient, if the standard deviation of the apriori

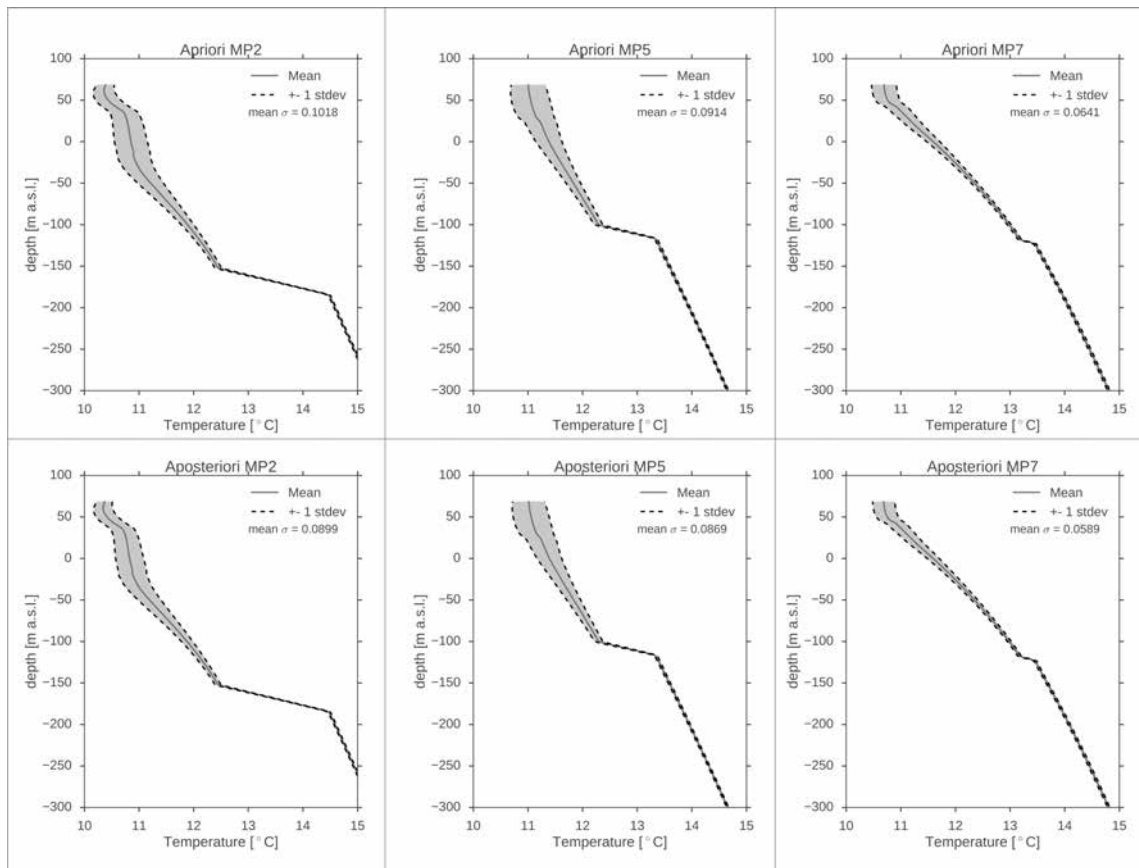


Figure 13: Mean and standard deviation of apriori and aposteriori distributions in simulated temperatures at three selected monitoring points (see Fig. 12 for location).

ensemble is too small compared to the uncertainty of the measurement data u_H . The low spread of the results suggest, that heterogeneous permeability has a minor impact on the simulation results, compared to hydraulic head boundary conditions, thermal conductivity of the units, and a transient signal of paleoclimate. The latter parameters were already obtained and optimized during the calibration step. Thus, results of the MonteCarlo simulations are valuable for the BHE model in Task 4.2.

6.3 Variations in groundwater flow

Similar to variations in temperature, groundwater velocity and direction does not vary significantly within the ensemble. According to equation (1), permeability is a governing parameter for Darcy-flow, similar to the difference in hydraulic head. Figure 14 shows a xy-slice (at around 30m depth below surface) with mean and standard deviation of groundwater velocity in y direction. Overall regional groundwater flow is predominantly from south to north (Fig. 14), as a result from the applied boundary conditions. Fluid flowrates increase at fault intersections, where the effective pathway for water decreases due to the fault displacement. The y-component has the biggest effect on the velocity magnitude, to a lesser degree the x-component and z-component.

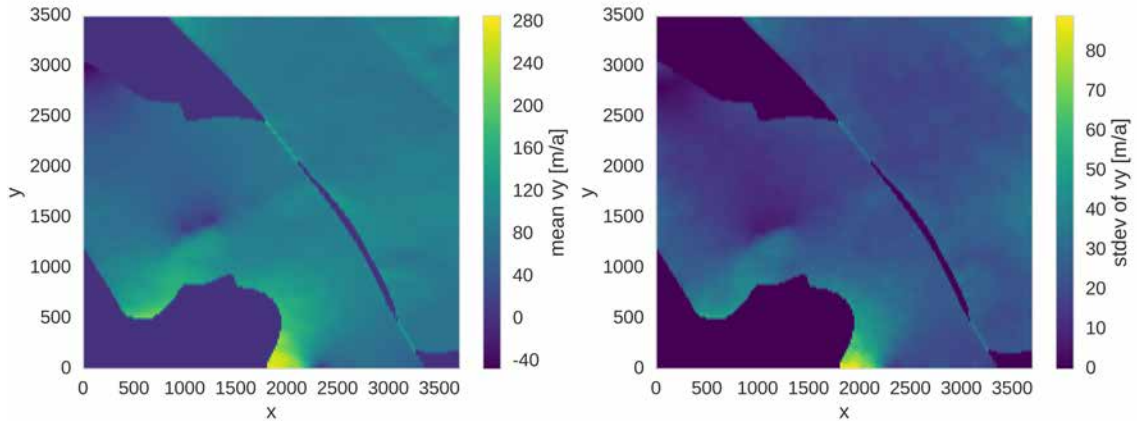


Figure 14: Mean and standard deviation of aposteriori y-direction velocity field in about 30 m depth below surface.

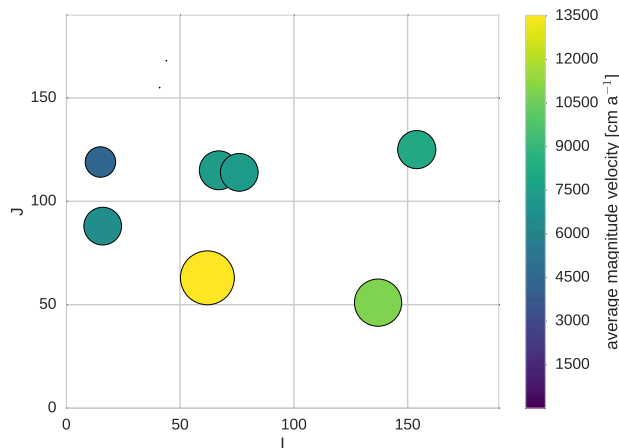


Figure 15: Mean and standard deviation at monitoring points

Average velocity magnitudes (color) and the connected standard deviations (size) at the monitoring points are shown in Figure 15. Note that monitoring points 1 and 2 show very low standard deviations (very small dots), but also low average velocity. Average velocity magnitude and the corresponding standard deviation are correlated. Groundwater velocities in the target area of the BHE model (around I:100 and J:140) are around 75 m a⁻¹.

7. Conclusion

The work done in Task 4.1 comprises the complete workflow from data-gathering to simulation and uncertainty assessment of a shallow geothermal reservoir system. The geological model built during Task 4.1 sufficiently represents the sedimentary structure of the subsurface in the study area. In particular the spatial resolution of aquitard-units, such as the lignite seam Morken are important for later flow simulations. The geological model was discretized in a big model covering an area of about 150 km².

Multiple temperature measurements in the study area (stars in Fig. 2) were used to calibrate this model using a gradient based bayesian inversion. The resulting parameters and boundary conditions were applied to a more detailed flow-model, and MC-simulations were performed for assessing the impact of heterogeneous permeability on temperature and groundwater flow in the target area.

Results of the MC-study showed that variations of the simulation ensemble are within the observation uncertainty range. Thus, a rejection algorithm based on the metropolis acceptance probability did not yield a satisfying reduction of the apriori ensemble.

However, due to a reasonable good model calibration, and an overall satisfying fit of the ensemble to observations in groundwater level, we can conclude that the average results of the MC-study are applicable as boundary conditions for a borehole heat exchanger model (BHE-model) simulated in Task 4.2. Overall, the results of this Task are motivating to continue by generating a highly detailed model of the subsurface of a settlement (blue polygon in Fig. 2) for simulating operation of a BHE-field.

References

- Clauser, C., 2003. *Numerical Simulation of Reactive Flow in Hot Aquifers: SHEMAT and Processing SHEMAT.*, Springer.
- Clauser, C. & Mareschal, J.-C., 1995. Ground temperature history in central europe from borehole temperature data, *Geophysical Journal International*, **121**(3), 805–817.
- Jorand, R., Clauser, C., Marquart, G., & Pechinig, R., 2015. Statistically reliable petrophysical properties of potential reservoir rocks for geothermal energy use and their relation to lithostratigraphy and rock composition: The ne rhenish massif and the lower rhine embayment (germany), *Geothermics*, **53**, 413–428.
- Rath, V., Wolf, A., & Bucker, H., 2006. Joint three-dimensional inversion of coupled groundwater flow and heat transfer based on automatic differentiation: sensitivity calculation, verification, and synthetic examples, *Geophysical Journal International*, **167**(1), 453–466.